# Theory of acoustophoresis in counterpropagating surface acoustic wave fields for particle separation

Zixing Liu, Guangyao Xu, Zhengyang Ni, Xizhou Chen, and Xiasheng Guo*
*Key Laboratory of Modern Acoustics (MOE), School of Physics, Collaborative Innovation Center of Advanced Microstructure, Nanjing University, Nanjing 210093, China*

Juan Tu and Dong Zhang†
*Key Laboratory of Modern Acoustics (MOE), School of Physics, Collaborative Innovation Center of Advanced Microstructure, Nanjing University, Nanjing 210093, China*
*and The State Key Laboratory of Acoustics, Chinese Academy of Science, Beijing 100190, China*

(Received 9 September 2020; accepted 15 February 2021; published 15 March 2021)

Acousotophoretic particle separations in counterpropagating surface acoustic wave (SAW) fields, e.g., standing SAWs (SSAWs), phase modulated SSAWs, tilted angle SSAWs, and partial standing SAWs, have proven successful. But there still lacks analytical tools for predicting the particle trajectory and optimizing the device designs. Here, we study the acoustophoresis of spherical Rayleigh particles in counterpropagating SAW fields and find that particle motions can be characterized into two distinct modes, the drift mode and the locked mode. Through theoretical studies, we provide analytical expressions of particle trajectories in different fields and different moving patterns. Based on these, we obtain theory-based protocols for designing such SAW acoustofluidic particle separation chips, which are demonstrated through finite-element simulations. The results here provide theoretical guidelines for designing high throughput and high efficiency particle separation devices.

DOI: 10.1103/PhysRevE.103.033104

## I. INTRODUCTION

Among the most successful applications of acoustofluidics is particle separation using surface acoustic waves (SAWs) [1], which employs high-frequency ultrasound to achieve good spatial precision, and can be easily integrated with optical microscopy [2] and peripheral circuits [3]. In sorting particles like cells, SAW fields load acoustic radiation force (ARF) on targets through wave leakage at the substrate-fluid interfaces [3,4]. SAWs activated by on-chip interdigital transducers (IDTs) establish traveling [5], standing [6], or more complicated [7,8] wave fields in long channels where exist constant fluid flows, and different mechanisms help to achieve the goal.

In a homogeneous liquid, the ARF acting on a spherical particle is highly dependent on its size [9], hence a traveling wave can move particles of different radii at distinct acceleration [5]. Despite this, standing SAW (SSAW) fields are preferred since the ARF therein can be magnitudes stronger [1]. Commonly, two counterpropagating planar SAWs of identical frequency and pressure amplitudes generate periodically distributed node and antinode lines staggered along the sound path, which respectively correspond to traps and barriers of the Gor'kov potential for particles of positive contrast factors [10], and on the contrary if the factors are negative. Thereby, particles move toward the trap lines at different acceleration, and are separated during migration, usually based on their sizes [2,6]. The maximum separating distance is a quarter of the SAW wavelength [11].

One way to break this limit is to use a phase modulated SSAW (PM-SSAW) field, where a varying phase difference between the two beams move the traps and barriers accordingly [12,13]. While all particles go forward with the fluid flow, the big ones move laterally faster than the small ones, leading to extended maximum separation distances. Another approach adopts a tilted angle SSAW (TaSSAW) field, where the wave front is tilted against the flow direction [11,14,15]. While the flow carries small particles ahead, it also helps big particles to cross the potential barriers and diverge from their original paths. It can also be helpful, if the IDTs are not tilted, to let the two waves have different amplitudes [16], or to establish a partial standing SAW (pSSAW) field. In this case, the overall field consists of a standing part and a traveling part, whereas the latter helps big particles to overcome the Gor'kov potential barriers [17].

All these methods aim at generating distinctive trajectories for different particles, and designing these separation chips should be based on the dynamics and kinematics of particles in the SAW fields. There are some preliminary studies for researchers to refer to. For example, the motion trajectory of a spherical particle in a standing field has been theoretically studied by Bruus [10] and Liu *et al*. [18] For a PM-SSAW field, Simon *et al*. [13] described the particles' drift mode motions through analytical predictions. In a TaSSAW field, Riaud *et al*. [19] obtained the slope of particle trajectories.

However, in designing particle separation acoustofluidics, few have benefited from these findings. The fact is, particle behaviors in such chips can be far more complicated than

*guoxs@nju.edu.cn
†dzhang@nju.edu.cn

 

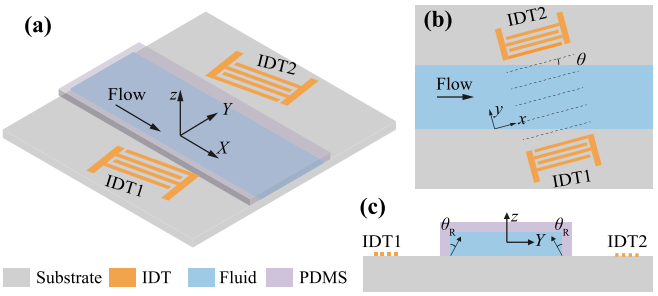


FIG. 1. (a) Schematic of the particle separation chip. (b) The top view and (c) the $Y$-$z$ cross section.

those predicted by the models [20,21]. For example, the device performance can be affected by the channel size, the IDT apertures, the tilted angle, the phase modulation rate, and the flow rate among other factors [13,15,22]. As a result, researchers resort to personal experiences or trial and error practices for problem solving [23], which limits further explorations of more delicate and effective functionalities of the devices.

The current work sets up a theoretical framework of acoustophoresis in counterpropagating SAW fields. From the kinematics of spherical Rayleigh particles, different factors are considered for predicting particle trajectories. The results indicate that particle moving patterns can be classified into two categories, between which a clear-cut transition condition exists. Based on the theories and finite-element (FE) analysis here, it is easy to find out how relevant devices can be optimized during designing and better performed after fabrication.

## II. THEORIES AND METHODS

### A. The SAW separation chip

A common SAW particle separation chip is illustrated in Fig. 1(a). On a piezoelectric substrate, a constant fluid flow moves along the $+X$ direction in a long channel. Two IDTs are fabricated on the substrate on both sides of the channel, with all the fingers along the $x$ axis. As shown in Fig. 1(b), the transducer coordinate $(x, y, z)$ is a rotation of the channel coordinate $(X, Y, z)$ by an angle $\theta$ $(0 \leqslant \theta < \frac{\pi}{2})$. The IDTs establish counterpropagating SAWs along the substrate, covering the area $x = 0$-$W_{\mathrm{IDT}}$, which leak into the fluid at $\theta_{\mathrm{R}} = \sin^{-1}(c_0/c_{\mathrm{S}})$ [4] with $c_{\mathrm{S}}$ being the SAW speed in the substrate and $c_0$ the speed of sound in the fluid, see Fig. 1(c). In the following, subscripts $x$, $y$, $z$ and $X$, $Y$ are used to represent corresponding components of vectors.

As the IDTs emit SAWs of angular frequency $\omega = 2\pi f$, $f$ being the frequency, the in-fluid pressure field is

$$p_{\mathrm{in}} = p_{\mathrm{I}} + p_{\mathrm{II}} = e^{-i\omega t + ik_z z}(p_1 e^{ik_y y} - p_2 e^{-ik_y y + i\varphi}), \quad (1)$$

where $i = (-1)^{\frac{1}{2}}$, $t$ is the time, $p_{\mathrm{I}}$ and $p_{\mathrm{II}}$ are the pressure waves generated by IDT1 and IDT2, whose amplitudes are $p_1$ and $p_2$ $(p_1 \geqslant p_2)$, respectively. The $y$ and $z$ components of the wave number $k = \omega/c_0$ are $k_y = k \sin\theta_{\mathrm{R}}$ and $k_z = k \cos\theta_{\mathrm{R}}$. $\varphi = \varphi(t)$ is a time-dependent phase difference between $p_{\mathrm{I}}$ and $p_{\mathrm{II}}$.

The device can be categorized as

(a) SSAW for $p_1 = p_2 \neq 0$, $\dot{\varphi} = d\varphi/dt = 0$, and $\theta = 0$,
(b) TaSSAW for $p_1 = p_2 \neq 0$, $\dot{\varphi} = 0$, and $\theta \neq 0$,
(c) PM-SSAW for $p_1 = p_2 \neq 0$, $\dot{\varphi} \neq 0$, and $\theta = 0$, and
(d) pSSAW for $p_1 > p_2$, $p_1$, $p_2 \neq 0$, $\dot{\varphi} = 0$, and $\theta = 0$.

### B. Model assumptions

The ARF expression we use is limited by neglect of wave reflections at the channel interfaces [21,24], as well as edge effects originated at the lower channel corners [25]. The boundary reflections can be reduced by adopting channel materials which have acoustic impedance comparable to that of the fluid and exhibit high damping. For example, the reflection coefficient from a water-glycerol mixture to Polydimethylsiloxane (PDMS) is only 0.06 [24], and a 2-mm PDMS layer can eliminate all waves traveling through it [21]. To reduce the edge effects, the manipulation area should be away from the side boundaries of the channel by a distance $h \tan\theta_{\mathrm{R}}$ ($h$ is the height of the channel, $\theta_{\mathrm{R}}$ is the Rayleigh angle) [23], and this is also helpful for weakening the impact of interface reflections and uneven flows. Nevertheless, one is recommended to carefully calibrate each device and make sure force distribution at the particle plane is as expected, e.g., by using particle image velocimetry [18].

The Stokes drage force (DF) we describe in the following can be enhanced by a factor $\chi$ by the channel walls [26,27]. This makes the particle motions much more complicated, especially when there is no general analytical form for $\chi$ [27]. Here we provide a simple estimation where a particle is located at a distance $\Delta$ away from the wall. As it moves parallel or perpendicular to the wall, $\chi$ is 1.126 or 1.285 for $\Delta = 5a$, 1.059 or 1.126 for $\Delta = 10a$, and 1.029 or 1.060 for $\Delta = 20a$, where $a$ is the particle radius. In applying the current theory, one needs to make the particles at least $10a$ away from all the channel boundaries (including the sidewalls, the substrate, and the lid), such that $\chi \approx 1$. For simplicity, the heights of the channels are not considered in this study.

Acoustic streaming (AS) is neglected in the analysis of acoustophoresis. To make this justifiable, particle motions should be dominated by the ARF and the fluid flow, while the AS velocity is negligibly low. In acoustophoresis where the flow is absent, a particle moves under the domination of ARF as soon as its size far exceeds the thickness of the viscous boundary layer, $\delta$ [28,29]. In water-filled channels which are used here, $\delta$ is estimated as 0.24 $\mu$m for 5-MHz fields, and $a$ being bigger than a critical radius 1.2 $\mu$m makes AS less important. Since SAW devices usually work at higher frequencies [21], this critical radius can be even smaller, i.e., 0.73 and 0.60 $\mu$m for the 13.3- and 19.97-MHz fields we used. Besides, the AS velocity, typical value can be $\sim$45 $\mu$m/s in a 13.45-MHz SSAW field [18], is usually much lower than the flow velocity used in this work ($v_{\mathrm{f}} = 1.5$ mm/s). Therefore, neglect of AS is reasonable here.

We only consider compressible particles in a viscous fluid. When the thermoviscous effect or viscoelastic particles are considered, the ARF theory should be updated by referring to Refs. [30] and [31].

### C. The ARF

Inside an acoustofluidic channel, particle motions are dominated by the ARF and/or the DF [20]. The classical theory of

ARF was developed by King [32], Yosioka [33], Hasegawa [9,17], and others. Gor'kov proposed the theory for small particles [34], which was then corrected by Settnes and Karlsen from the Bruus group to account for fluid viscousity [35] and thermoviscousity [30]. In SAW devices, the ARF is related to the Rayleigh angle [13,36].

For a compressible spherical particle of Rayleigh size, the ARF ($\boldsymbol{F}^{\mathrm{rad}}$) acting on it can be described using the multipole expansion theory [10]. In the field given by Eq. (1), the $y$ component ARF is

$$F_y^{\mathrm{rad}} = -\pi a^3 \left\{ \frac{2\kappa_0}{3} \mathrm{Re}\left( f_1^* p_{\mathrm{in}}^* \frac{\partial p_{\mathrm{in}}}{\partial y} \right) - \rho_0 \mathrm{Re}\left[ f_2^* \left( v_{\mathrm{in},y}^* \frac{\partial v_{\mathrm{in},y}}{\partial y} + v_{\mathrm{in},z}^* \frac{\partial v_{\mathrm{in},y}}{\partial z} \right) \right] \right\}, \quad (2)$$

where $\kappa_0 = 1/\rho_0 c_0^2$ is the compressibility of the fluid, with $\rho_0$ being its density. $\boldsymbol{v}_{\mathrm{in}}$ is the velocity field of the incident wave. $\mathrm{Re}(\cdot)$ and an asterisk refer to the real part and conjugate of a complex variable. The monopole and dipole scattering coefficients $f_1$ and $f_2$ are [35]

$$f_1 = 1 - \frac{\kappa_{\mathrm{p}}}{\kappa_0}, \quad f_2 = \frac{2(1-\gamma)(\rho_{\mathrm{p}} - \rho_0)}{2\rho_{\mathrm{p}} + \rho_0 - 3\rho_0\gamma}, \quad (3)$$

in which

$$\gamma = -3[1 + i(1 + \delta/a)]\delta/2a. \quad (4)$$

Here, $\kappa_{\mathrm{p}} = 1/\rho_{\mathrm{p}} c_{\mathrm{p}}^2$ is the compressibility of the particle, with $\rho_{\mathrm{p}}$ and $c_{\mathrm{p}}$ being its density and speed of sound. $\delta = (2\eta/\rho_0\omega)^{\frac{1}{2}}$ is the thickness of the viscous boundary layer where $\eta$ is the dynamic viscosity of the fluid. The $y$- and $z$- components of the velocity field in Eq. (2) are

$$v_{\mathrm{in},y} = -\frac{1}{\rho_0}\int \frac{\partial p_{\mathrm{in}}}{\partial y} dt = \frac{k_y}{\rho_0}\left( \frac{p_{\mathrm{I}}}{\omega} - \frac{p_{\mathrm{II}}}{\omega - \dot{\varphi}} \right),$$
$$v_{\mathrm{in},z} = -\frac{1}{\rho_0}\int \frac{\partial p_{\mathrm{in}}}{\partial z} dt = \frac{k_z}{\rho_0}\left( \frac{p_{\mathrm{I}}}{\omega} + \frac{p_{\mathrm{II}}}{\omega - \dot{\varphi}} \right). \quad (5)$$

Since $\varphi(t)$ is usually generated by slightly shifting the working frequency of either IDT [7,12], here $\dot{\varphi}$ is considered as a constant much smaller than $\omega$. Substituting Eqs. (1) and (5) into Eq. (2) thus yields

$$F_y^{\mathrm{rad}} \approx \pi a^3 k_y [E_{\mathrm{a,t}} \mathrm{Im}(f_2) - 4E_{\mathrm{a,s}} \Phi \sin(2k_y y - \varphi)], \quad (6)$$

where $\mathrm{Im}(f_2)$ is the imaginary part of $f_2$, $\Phi = f_1/3 + \mathrm{Re}(f_2)(k_y^2 - k_z^2)/2k^2$ is the acoustic contrast factor [10,13]. $E_{\mathrm{a,s}} = p_1 p_2/(\rho_0 c_0^2)$ and $E_{\mathrm{a,t}} = (p_1^2 - p_2^2)/(\rho_0 c_0^2)$ are the acoustic energy densities of the standing and traveling parts of the field, respectively, with their equivalent pressure amplitudes being $2(p_1 p_2)^{\frac{1}{2}}$ and $(p_1^2 - p_2^2)^{\frac{1}{2}}$. When considering the thermoviscous effect or viscoelastic particles, $f_1$ in the expression of $\Phi$ becomes $\mathrm{Re}(f_1)$, while $\mathrm{Im}(f_2)$ in Eq. (6) should be replaced with $-\frac{2}{3}\mathrm{Im}(f_1) + \mathrm{Im}(f_2)$ [30,31].

Equation (6) degrades to the formula derived by Settens and Bruus [35] for BAW acoustofluidics when $\theta_{\mathrm{R}} = 0$, and is consistent with the expression given by Simon *et al.* [13] and Shen *et al.* [36] for SSAW considering $ka \ll 1$. As for $p_1 = p_2$ and $\dot{\varphi}$ being a constant, Eq. (6) is identical to the force expression in PM-SSAW fields [13].

### D. Particle acoustophoresis

An acoustophoretic particle also experiences a DF, which is [27] $\boldsymbol{F}_{\mathrm{drag}} = 6\pi\eta a(\boldsymbol{v}_{\mathrm{f}} - \boldsymbol{v}_{\mathrm{p}})$. $\boldsymbol{v}_{\mathrm{f}}$ and $\boldsymbol{v}_{\mathrm{p}}$ are the velocity of the fluid and the particle, respectively, with their amplitudes being $v_{\mathrm{f}}$ and $v_{\mathrm{p}}$. Considering the AS being negligible compared to the flow [29], dynamic equations of the particle motion are

$$6\pi\eta a(v_{\mathrm{f}}\cos\theta - v_{\mathrm{p},x}) = \frac{4}{3}\pi\rho_{\mathrm{p}} a^3 \frac{dv_{\mathrm{p},x}}{dt},$$
$$F_y^{\mathrm{rad}} + 6\pi\eta a(-v_{\mathrm{f}}\sin\theta - v_{\mathrm{p},y}) = \frac{4}{3}\pi\rho_{\mathrm{p}} a^3 \frac{dv_{\mathrm{p},y}}{dt}. \quad (7)$$

Since the timescale for accelerating a particle is far shorter than that for translating it, the inertial effect is neglected [13]. Substituting Eq. (6) into Eq. (7) and setting $\Psi_{\mathrm{s}} = 2k_y E_{\mathrm{a,s}}\Phi/3\eta$ and $\Psi_{\mathrm{t}} = k_y E_{\mathrm{a,t}}\mathrm{Im}(f_2)/6\eta$ yields

$$\frac{dx}{dt} = v_{\mathrm{f}}\cos\theta, \quad (8)$$

$$\frac{dy}{dt} = \Psi_{\mathrm{t}} a^2 - \Psi_{\mathrm{s}} a^2 \sin(2k_y y - \varphi) - v_{\mathrm{f}}\sin\theta. \quad (9)$$

Time integral on Eq. (8) gives $x = v_{\mathrm{f}} t\cos\theta$ (the integration constant is zero as the particle enters the field at $x = 0$). Since Eq. (9) is a separable variable equation, it can be rewritten as

$$-2k_y v_{\mathrm{f}} dt = \frac{d(2k_y y - \varphi)}{b_d + b_l \sin(2k_y y - \varphi)}, \quad (10)$$

in which

$$b_d = \sin\theta - \frac{\Psi_{\mathrm{t}} a^2}{v_{\mathrm{f}}} + \frac{\dot{\varphi}}{2k_y v_{\mathrm{f}}}, \quad b_l = \frac{\Psi_{\mathrm{s}} a^2}{v_{\mathrm{f}}}. \quad (11)$$

Here $b_d$ is named the drifting factor, which is related to the tilted angle, the traveling part ARF and the rate of phase modulation; $b_l$, the locking factor, is the ratio of the standing part ARF to the DF. In the following, we assume $b_l$ and $b_d$ are constants, this in turn implies $\dot{\varphi}$ to be a constant.

When $b_d = 0$, time integral on Eq. (10) gives [10,13]

$$y = \frac{1}{k_y}\tan^{-1}[\tan(k_y y_0) e^{-2k_y \Psi_{\mathrm{s}} a^2 t}], \quad (12)$$

where $y_0$ is the initial $y$ position of the particle. For $b_d \neq 0$, time integral on Eq. (10) is dependent on $|b_d/b_l|$. In cases where $|b_d/b_l| > 1$, the integral yields

$$-\beta k_y v_{\mathrm{f}} t = \xi_1(y, \varphi) - \xi_1(y_0, \varphi_0), \quad (13)$$

where $\varphi_0 = \varphi|_{t=0}$ is between $-\pi$ and $\pi$, $\beta = |b_d^2 - b_l^2|^{\frac{1}{2}}$, and

$$\xi_1(y, \varphi) = \tan^{-1}\left[ \frac{b_d}{\beta}\tan\left( k_y y - \frac{\varphi}{2} \right) + \frac{b_l}{\beta} \right]. \quad (14)$$

The $y$ position of the particle is then determined as

$$y = \frac{\varphi}{2k_y} + \frac{1}{k_y}\tan^{-1}\left\{ \frac{\beta}{b_d}\tan[\xi_1(y_0, \varphi_0) - \beta k_y v_{\mathrm{f}} t] - \frac{b_l}{b_d} \right\}. \quad (15)$$

Equation (15) is similar to the trajectory expression given by Pelton *et al.* for particles in a sinusoidally distributed optical force field [37], which is well expected. This analogy was first reported by Riaud *et al.* [19] It is worth noting that Eq. (15) cannot describe the full timeline of acoutophoresis

since the value of the arctangent function is limited to $-\frac{\pi}{2}$ to $\frac{\pi}{2}$ even if $t$ goes to infinity. To fix this problem, the $y$-$t$ curve should be unwrapped as is done in signal processing. Specifically, Eq. (15) can be solved by assigning $y_0 = y$ as soon as $\tan[\xi_1(y_0, \varphi_0) - \beta k_y v_f t]$ approaches $\pm\infty$. It is then interesting to find that, as the locking part of the field moves by a $y$ distance $\dot{\varphi}t/2k_y$, which is a linear function of the time $t$, the particle cannot be effectively captured by a certain trap. Dominated by the drifting part of the field, it can drift from one potential trap to another in an oscillatory manner. This moving pattern is categorized as a drift mode [19].

For $|b_d/b_l| < 1$, time integral on Eq. (10) gives

$$-\beta k_y v_f t = \xi_2(y, \varphi) - \xi_2(y_0, \varphi_0), \tag{16}$$

where

$$\xi_2(y, \varphi) = \frac{1}{2}\ln|C(y, \varphi)|,$$
$$C(y, \varphi) = \frac{b_d \tan(k_y y - \varphi/2) + b_l - \beta}{b_d \tan(k_y y - \varphi/2) + b_l + \beta}. \tag{17}$$

The analytic particle trajectory then differs depending on the sign of $C(y_0, \varphi_0)$. For $C(y_0, \varphi_0) < 0$ and $C(y_0, \varphi_0) > 0$, one respectively has

$$y = \frac{\varphi}{2k_y} + \frac{1}{k_y}\tan^{-1}\left\{\frac{\beta}{b_d}\tanh[\beta k_y v_f t - \xi_2(y_0, \varphi_0)] - \frac{b_l}{b_d}\right\}, \tag{18a}$$

$$y = \frac{\varphi}{2k_y} + \frac{1}{k_y}\tan^{-1}\left\{\frac{\beta}{b_d}\coth[\beta k_y v_f t - \xi_2(y_0, \varphi_0)] - \frac{b_l}{b_d}\right\}. \tag{18b}$$

There is actually no big difference between Eqs. (18a) and (18b) since both the `tanh` and `coth` functions approach unity as $t$ increases. Hence, $y$ is a monotonic function of $t$, and the particle location will finally approach a fixed distance ($y_e$) below the trap line at $\varphi/2k_y$,

$$y_e = \frac{1}{k_y}\tan^{-1}\left(\frac{\beta - b_l}{b_d}\right). \tag{19}$$

Therefore, the particle cannot overcome a potential barrier to approach neighboring traps, but will be captured at an equilibrium position. This moving pattern is classified as a locked mode [19].

### E. FE simulations and material parameters

In the following, particle trajectories and separations in counterpropagating SAW fields will be discussed based on the theories given in the above. The initial phase $\varphi_0$ is set as zero except in PM-SSAW devices, since it is always easy to place the origin on a node line of the field.

FE simulations using COMSOL Multiphysics (v5.4, COMSOL, Sweden) are carried out to validate some key results. In the models, we only consider the acoustic field and the background flow field within the channel area in the $X$-$Y$ plane, and an out-of-plane wave number $k_z$ is introduced to describe wave leakage from the substrate (128° $Y$-$X$ $LiNbO_3$). PDMS channel walls are described as impedance boundaries [20,21]. In water-filled channels, particles of different sizes to be separated can be made of Polystyrene (PS) or Pyrex (PY), both having positive contrast factors. Table I lists the material parameters shared by all the calculations and models. More details about the simulation are given in Appendix A.

TABLE I. Material parameters.

| | Description | Symbol | Value |
|---|---|---|---|
| Water [28] | Density | $\rho_0$ | 998 kg/m$^3$ |
| | Speed of sound | $c_0$ | 1495 m/s |
| | Compressibility | $\kappa_0$ | 448 TPa$^{-1}$ |
| | Viscosity | $\eta$ | 0.893 mPa s |
| Polystyrene [28] | Density | $\rho_{ps}$ | 1050 kg/m$^3$ |
| | Compressibility | $\kappa_{ps}$ | 249 TPa$^{-1}$ |
| PDMS [38] | Density | $\rho_{pm}$ | 1030.5 kg/m$^3$ |
| | Longitudinal wave speed | $c_{pm}$ | 1035 m/s |
| Pyrex [35] | Density | $\rho_{py}$ | 2230 kg/m$^3$ |
| | Compressibility | $\kappa_{py}$ | 27.8 TPa$^{-1}$ |
| $LiNbO_3$ [20] | SAW speed | $c_S$ | 3994 m/s |

## III. RESULTS

### A. Acoustophoresis in SSAWs

An SSAW field is widely used in the early models of particle separation acoustofluidics [2,6]. Since $\theta = 0$, the $(X, Y, z)$ coordinate overlaps with $(x, y, z)$. Acoustophoresis therein has been broadly discussed elsewhere [2,10], and is briefly described here.

According to Eq. (12), how a particle moves in a given SSAW field depends on its $\Phi a^2$ value. As is mentioned in Ref. [39], particles should enter the field slightly away from a barrier line, and will reach the neighborhood of a trap, e.g., from $\lambda_S/4 - y_{c0}$ to $y_c$ ($\lambda_S = 2\pi/k_y$ is the SAW wavelength), where $y_c$ is much smaller than $\lambda_S$ [39].

Here, we examine PS beads of different radii entering an SSAW field of $f = 13.3$ MHz and $p_1 = p_2 = 100$ kPa at $Y = y_0 = \lambda_S/4 - \lambda_S/40$ ($\lambda_S = 300\ \mu$m) where the flow velocity $v_f = 1.5$ mm/s, and plot the trajectories in Fig. 2. Obviously, bigger particles arrive at the $Y = 0$ trap faster, and it is natural to optimize the separation distance by controlling the period that the particles stay in the field, e.g., by adjusting $v_f$ or $W_{IDT}$.

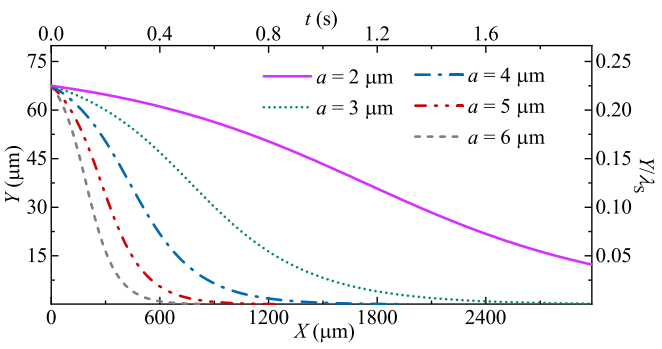


FIG. 2. Trajectories of different radii PS beads in an SSAW field of $f = 13.3$ MHz, $p_1 = p_2 = 100$ kPa and $v_f = 1.5$ mm/s. The particles enter the field at $X = 0$, $Y = \lambda_S/4 - \lambda_S/40$.

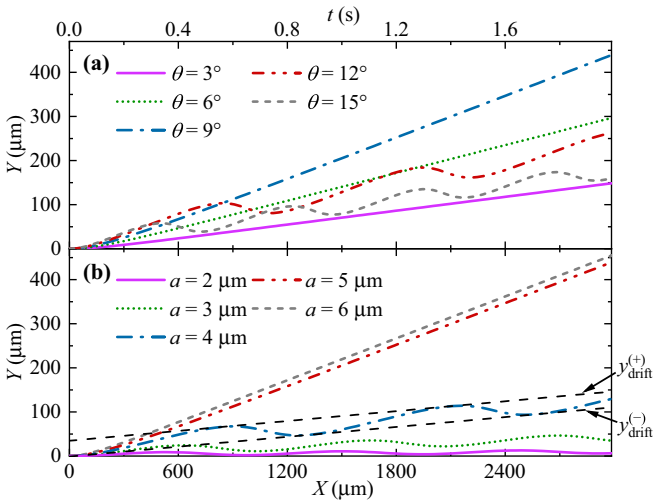


FIG. 3. The trajectories in TaSSAW fields for (a) 5-$\mu$m PS beads at different tilted angle $\theta$, and (b) particles of different radii at $\theta = 9°$. The dashed lines in panel (b) are the trajectory boundaries of the 4-$\mu$m particles.

### B. Acoustophoresis in TaSSAWs

In a TaSSAW field, the $(X, Y, z)$ coordinate is a rotation of $(x, y, z)$. These devices require $p_1 = p_2$, $\dot{\varphi} = 0$ and $0 < \theta < \frac{\pi}{2}$. The particle trajectories in $(x, y, z)$ can be determined using Eqs. (15) and (18), where $b_d = \sin\theta$.

The acoustophoretic pattern is determined by the capability of the DF to overwhelm the ARF. If $a$ and $v_f$ are given, $b_d = b_l$ gives the transition condition between the locked and drift modes as a critical value of the tilted angle, the flow velocity, or the particle radius,

$$\theta_c = \sin^{-1}\frac{\Psi_s a^2}{v_f},\ v_c = \frac{\Psi_s a^2}{\sin\theta},\ a_c = \left(\frac{v_f \sin\theta}{\Psi_s}\right)^{\frac{1}{2}}. \tag{20}$$

The critical tilted angle $\theta_c$ is equivalent to the condition given by Riaud *et al.* [19]

For example, let an $a = 5$ $\mu$m PS bead enter a TaSSAW field of $f = 13.3$ MHz, $p_1 = p_2 = 100$ kPa at $x = 0$, $y = 0$. At $v_f = 1.5$ mm/s, $\theta_c$ is determined as 9.14°. In the trajectories plotted in Fig. 3(a), the $\theta = 3°$, 6°, and 9° cases allow the particle to be "locked," and the trajectories are almost straight lines parallel to the traps. By further increasing $\theta$ to 12° and 15°, the traps fail to catch the particle which follows oscillatory patterns and drifts across potential barriers repeatedly.

At $\theta = 9°$ and $v_f = 1.5$ mm/s, particle trajectories corresponding to $a = 2$, 3, 4, 5, and 6 $\mu$m are given in Fig. 3(b), where the 5- and 6-$\mu$m ones are in locked modes, and the rest drift repeatedly since their radii are below $a_c = 4.96\,\mu$m. After moving along the channel for 2.7 mm, the separation distance between the 3- and 5-$\mu$m particles is about 350 $\mu$m, exceeding the SAW wavelength (300 $\mu$m). In Fig. 3, all trajectories are transformed from $(x, y, z)$ to $(X, Y, z)$.

It is obvious from Eq. (18) that, as the time goes by, the trajectory of a "locked" particle approaches

$$y_{\text{locked}} = \frac{\varphi_0}{2k_y} + y_e, \tag{21}$$

i.e., the trajectory is independent of $x$. Since the initial position $y_0$ is unimportant as indicated by Eq. (21), and $\varphi_0$ can be kept constant for all particles through prefocusing [1,23], it is easy to conclude that all locked particles move along similar paths; see Fig. 3(b).

For particles in drift modes, Eq. (15) gives their trajectory boundaries in the $x$-$y$ plane as

$$y^{(\pm)}_{\text{drift}} = \frac{1}{2k_y}\left[\frac{-2k_y\beta x}{\cos\theta} + \varphi_0 + 2\xi_1(y_0, \varphi_0)\right] \pm \delta_y^{\pm}, \tag{22}$$

where

$$\delta_y^{\pm} = \frac{1}{k_y}\tan^{-1}\frac{(1-\cos\alpha)^{3/2}}{(8\cos\alpha)^{1/2} \pm (1+\cos\alpha)^{3/2}}, \tag{23}$$

and $\alpha = \sin^{-1}(b_l/b_d)$. On top of the earlier work of Riaud *et al.* where the deflection angle of a particle line is reported, Eq. (22) provides an explicit expression of the trajectory. Here, the contributions of $y_0$ and $\varphi_0$ are included, and the boundaries of the oscillatory trajectories are clarified. For the derivation of the parameter $\delta_y^{\pm}$, see Appendix B. In Fig. 3(b), $y^{(\pm)}_{\text{drift}}$ are marked for the 4-$\mu$m particles, where the initial conditions $\varphi_0 = 0$ and $y_0 = 0$ can be easily achieved through prefocusing.

### C. Acoustophoresis in PM-SSAWs

In a PM-SSAW device, $p_1 = p_2$, $\theta = 0$, and $\dot{\varphi} \neq 0$, and $(X, Y, z)$ again overlaps with $(x, y, z)$. The standing field moves along the $Y$ (or $y$) direction at a speed of $v_s = \dot{\varphi}/2k_y$, the drifting factor $b_d = \dot{\varphi}/(2k_y v_f) = v_s/v_f$.

Considering $t = x/v_f$, the particle trajectory in a drift and locked mode is described by Eqs. (15) and (18), respectively. The transition condition $b_d = b_l$ gives a critical phase modulation rate or a critical radius,

$$\dot{\varphi}_c = 2k_y\Psi_s a^2, \quad a_c = \left(\frac{\dot{\varphi}}{2k_y\Psi_s}\right)^{\frac{1}{2}}. \tag{24}$$

Here, $\dot{\varphi}_c$ is equivalent to the critical nodal translation speed given by Simon *et al.* [7] and the optimal rate given by Rhyou *et al.* [40]

For a PM-SSAW field of $f = 13.3$ MHz, $p_1 = p_2 = 100$ kPa, $v_f = 1.5$ mm/s, $\dot{\varphi}_c$ is determined as 9.98 rad/s for an $a = 5$ $\mu$m PS particle. Here we let the particle enter at $X = 0$ and $Y = 0$, and take $\varphi_0 = 0$. By varying $\dot{\varphi}$ from 3 to 15 rad/s, in Fig. 4(a) the trajectory slopes gradually approach $v_s/v_f$. At $\dot{\varphi} = 3$, 6, and 9 rad/s, the particle is "locked." As for $\dot{\varphi} = 12$ and 15 rad/s, the traps move fast and fail to catch the particle, which drifts from one trap to another. By fixing $\dot{\varphi} = 9$ rad/s, we have $a_c = 4.75$ $\mu$m, and particles having $a > a_c$ are "locked," while smaller ones follow drift patterns; see Fig. 4(b).

However, as a streamline of particles enter a PM-SSAW field at a fixed $y_0$ continuously, the initial phase $\varphi_0$ varies from one particle to another. For example, we let 3- and 5-$\mu$m PS particles enter the field where $\dot{\varphi} = 9$ rad/s, and make $\varphi_0$ randomly distributed from $-\pi$ to $\pi$. The results in Fig. 4(c) show that, variation in $\varphi_0$ does not change the particle moving patterns. However, instead of marching along line paths as shown in Figs. 4(a) and 4(b), each type of particles eventually

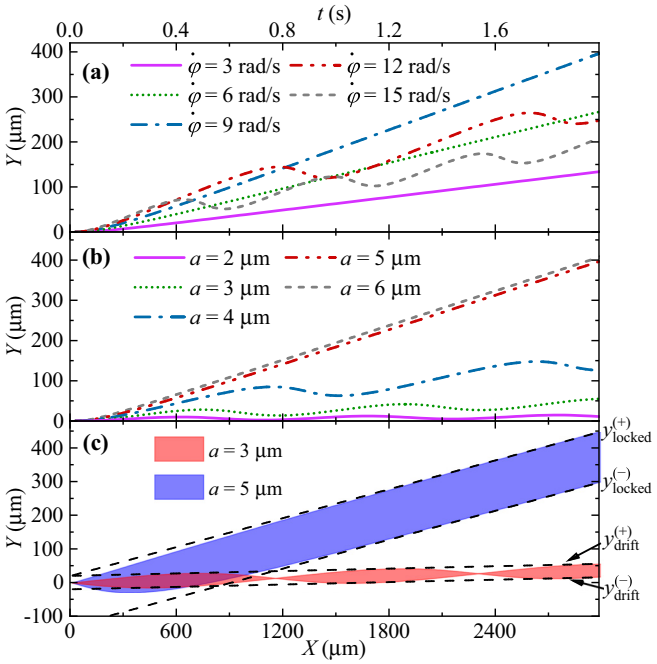


FIG. 4. Acoustophoresis of PS beads in a PM-SSAW field of $f = 13.3$ MHz, $p_1 = p_2 = 100$ kPa, and $v_f = 1.5$ mm/s. Trajectories of (a) a 5-$\mu$m particle at $\dot{\varphi} = 3$, 6, 9, 12, and 15 rad/s, $\varphi_0 = 0$, and (b) a 2-, 3-, 4-, 5-, and 6-$\mu$m particle at $\dot{\varphi} = 9$ rad/s, $\varphi_0 = 0$. (c) Trajectory bands (between dashed boundaries) of 3- and 5-$\mu$m particles at $\dot{\varphi} = 9$ rad/s, $\varphi_0$ is randomly distributed from $-\pi$ to $\pi$.

occupies a band, as is indicated by the shadowed patterns in Fig. 4(c).

Therefore, the trajectories in either modes are bounded by two straight lines. For the locked mode, they are

$$y^{(\pm)}_{\text{locked}} = y_0 + \frac{1}{k_y}\left(\frac{\dot{\varphi}x}{2v_f} + \tan^{-1}\frac{\beta}{b_d}\right) - \frac{\pi \mp \pi}{2k_y}, \tag{25}$$

i.e., the bands of "locked" particles have widths of $\lambda_S/2$ in the $y$ direction. In drift modes, the boundary lines are

$$y^{(\pm)}_{\text{drift}} = \frac{1}{2k_y}\left[\left(\frac{\dot{\varphi}}{v_f} - 2k_y\beta\right)x\right] + y_0 \pm \delta_y^{\pm} \pm \delta_y^{\mp}. \tag{26}$$

For more details about this expression, see Appendix B. In Fig. 4(c), the $y^{(\pm)}_{\text{locked}}$ and $y^{(\pm)}_{\text{drift}}$ boundaries are marked for the two types of particles.

### D. Acoustophoresis in pSSAWs

In a pSSAW device, $(X, Y, z)$ overlaps with $(x, y, z)$, the field can be characterized with an SWR $l = (p_1 + p_2)/(p_1 - p_2)$ [41]. Since $\theta = 0$, $\varphi = 0$ and $p_1 > p_2$, we have $b_d < 0$ here. It is convenient to assume there exists a standing wave part and a traveling wave part [17]. The former moves particles to trap lines, and the latter pushes them unilaterally [16]. Here, $|b_d/b_l| = |\text{Im}(f_2)/\Phi|l/(l^2 - 1)$.

We let a PY bead of $a = 1.5$ $\mu$m enter a pSSAW field of $f = 13.3$ MHz and $p_1 = 1$ MPa at $X = 0$, $Y = 0.2\lambda_S$, and plot its trajectories corresponding to different $l$ in Fig. 5(a). For $l = 1$, the locking part disappears, and the traveling field propagates along the $+Y$ direction. In this case, the particle advances

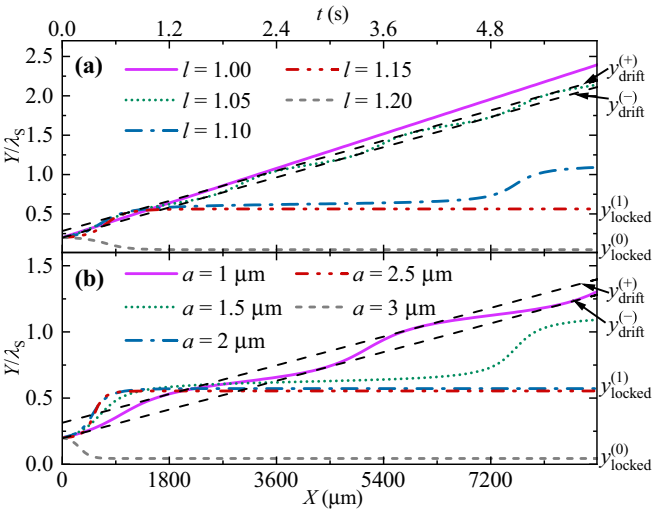


FIG. 5. Acoustophoresis of PY beads in a pSSAW field of $f = 13.3$ MHz, $p_1 = 1$ MPa, $v_f = 1.5$ mm/s. (a) $a = 1.5$ $\mu$m, $l = 1$, 1.05, 1.1, 1.15, and 1.2. (b) $a = 1$, 1.5, 2, 2.5, and 3 $\mu$m, $l = 1.1$. The black dashed lines are the trajectory boundaries for $a = 1.5$ $\mu$m, $l = 1.05$ in (a) and $a = 1$ $\mu$m, $l = 1.1$ in (b).

along a straight path, but is in neither of the modes since there are no traps and barriers. As $l$ increases to 1.05 and 1.1, the locking part arises, but is overwhelmed by the drifting part, and the particle moves in drift modes. By further increasing $l$ to 1.15 and 1.2, the particle is finally "locked" at $y = 0.563\lambda_S$ and $0.046\lambda_S$, respectively. The critical SWR is

$$l_c = \left|\frac{\text{Im}(f_2)}{2\Phi}\right| + \left[\left(\frac{\text{Im}(f_2)}{2\Phi}\right)^2 + 1\right]^{\frac{1}{2}}, \tag{27}$$

above which a locked mode is expected. Here $l_c$ is 1.105.

The particle radius also plays a part in determining its moving pattern, since $f_2$ and $\Phi$ are also dependent on $a$, see Sec. II C. However, extracting an analytical expression of the critical radius is difficult. Considering this, we examine the $|b_d/b_l| = 1$ condition numerically. For example, the current field combined with $l = 1.1$ gives a critical radius $a = 1.57$ $\mu$m, above which the particle is dominated by the locking part. As is observed in Fig. 5(b), the 2-, 2.5- and 3-$\mu$m particles are in locked modes, while the 1- and 1.5-$\mu$m ones move in drift modes.

It is interesting to find in Fig. 5(a) that, as the SWR changes from 1.15 to 1.2, the final locked position $y_{\text{locked}}$ of a particle can be moved from above $y_0$ to below $y_0$. Similarly, in Fig. 5(b), as $a$ changes from 2.5 $\mu$m to 3 $\mu$m, $y_{\text{locked}}$ also moves downwards. In fact, $y_{\text{locked}}$ is a position highly dependent on $y_0$ and $\varphi_0$. Specifically, with $C(y_0, \varphi_0) > 0$, $y_0$ and $\varphi_0$ satisfy

$$\frac{\varphi_0 + 2(n-1)\pi}{2k_y} - \frac{1}{k_y}\tan^{-1}\frac{\beta + b_l}{b_d} < y_0 < \frac{\varphi_0 + 2n\pi}{2k_y} + y_e, \tag{28}$$

where $n = -\infty \ldots \infty$ is an integer, and the trajectory expression is Eq. (18b). The particle moves upwards in the field,

finally approach

$$y_{\text{locked}}^{(n)} = \frac{\varphi_0 + 2n\pi}{2k_y} + y_e. \tag{29}$$

As for $C(y_0, \varphi_0) < 0$, the particle goes downwards, and Eq. (18a) should be adopted for trajectory predictions. Here, $y_0$ and $\varphi_0$ satisfy

$$\frac{\varphi_0 + 2n\pi}{2k_y} + y_e < y_0 < \frac{\varphi_0 + 2n\pi}{2k_y} - \frac{1}{k_y}\tan^{-1}\frac{\beta + b_l}{b_d}, \tag{30}$$

while the particle also approaches $y_{\text{locked}}^{(n)}$. Obviously, in Fig. 5(a), the $l = 1.15$ case moves the particle up to $y_{\text{locked}}^{(1)}$, $l = 1.2$ makes it go to $y_{\text{locked}}^{(0)}$; in Fig. 5(b), the 2.5-$\mu$m particle moves to $y_{\text{locked}}^{(1)}$, and the 3-$\mu$m particle goes to $y_{\text{locked}}^{(0)}$, as are marked in the figures.

The boundaries lines of the drift mode trajectories are

$$y_{\text{drift}}^{(\pm)} = \frac{1}{2k_y}[2k_y\beta x + \varphi_0 + 2\xi_1(y_0, \varphi_0)] \pm \delta_y^{\pm}, \tag{31}$$

where the $\delta_y^{\pm}$ defined in Eq. (23) should be updated by considering $\alpha = -\sin^{-1}(b_l/b_d)$ here. For demonstration, the boundaries for the $l = 1.05$ case in Fig. 5(a) and the 1-$\mu$m particle in Fig. 5(b) are marked with dashed lines.

## IV. DISCUSSION

In the studies of bulk acoustic wave (BAW) devices, optimization of particle separation in standing fields has been discussed elsewhere [42], where the influence of the initial position $y_0$ is revealed. Here, the impact of $y_0$ will be skipped, since (a) the conclusion should be similar to the BAW case, and (b) it is easy to set $y_0$ in SAW devices through prefocusing [22].

### A. Design of SSAW devices

We consider the SSAW chip used in Sec. III A. Assuming two types of monodispersed spherical beads of positive contrast factors, $P_j$ ($j = 1, 2$), are mixed for separation, while $\Phi_1 a_1^2 > \Phi_2 a_2^2$. From this step, the subscript $j$ is assigned to the parameters corresponding to particle $P_j$. As the particles enter the field at $X = 0$, $Y = y_0$, two particle lines can be observed, with their $X$-dependent lateral distance being $\Delta Y = |Y_1 - Y_2| - y_a$, $y_a = (a_1 + a_2)$.

Here, $y_0$ should be at the neighborhood of a barrier, such that the final separation distance $\Delta Y_c$ can be maximized. By taking $y_0 = \lambda_S/4 - y_{c0}$, one obtains

$$\Delta Y = \frac{1}{k_y}\{\tan^{-1}[\tan(k_y y_0)e^{-2k_y\Psi_{s,2}a_2^2 t}] - \tan^{-1}[\tan(k_y y_0)e^{-2k_y\Psi_{s,1}a_1^2 t}]\} - y_a. \tag{32}$$

As $t$ increases from 0, $P_1$ approaches the trap faster due to bigger ARF. But after a certain period, it slows down since the ARF declines, and $P_1$ can have lower velocity than $P_2$. That is, $\Delta Y$ should first increase then decrease. As an example, take the 6-$\mu$m and 2-$\mu$m PS beads as $P_1$ and $P_2$, respectively, and let them enter an SSAW field of $f = 13.3$ MHz, $p_1 = p_2 = 100$ kPa and $v_f = 1.5$ mm/s at $X = 0$, $Y = y_0 = \lambda_S/4 - \lambda_S/40$ ($y_{c0} = \lambda_S/40$). In Fig. 6(a), $\Delta Y$ maximizes to $0.174\lambda_S$ as $P_1$ moves close to $Y = 0$, and gradually decreases after that.

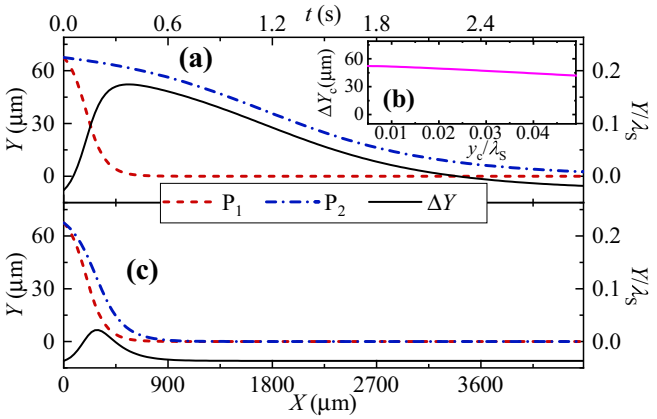


FIG. 6. Particle separation in an SSAW field of $f = 13.3$ MHz, $p_1 = p_2 = 100$ kPa. (a) Trajectories of the 6-$\mu$m and 2-$\mu$m particles and $\Delta Y$. (b) $\Delta Y_c$ as a function of $y_c$. (c) Trajectories of the 6-$\mu$m and 5-$\mu$m particles and $\Delta Y$.

It is necessary to determine the time $t_c$ when $\Delta Y$ maximizes. But an analytical expression of $t_c$ is difficult to obtain from Eq. (32). Here we estimate $t_c$ as the time $P_1$ migrates from $Y = \lambda_S/4 - \lambda_S/40$ to $y_c$, although this can cause inaccuracies. According to Eq. (12), we have [42]

$$t_c = -\frac{1}{2k_y a_1^2 \Psi_{s,1}}\ln\left[\frac{\tan(k_y y_c)}{\tan(k_y y_0)}\right], \tag{33}$$

hence $t_c$ is 0.256 s (here $y_c = y_{c0} = \lambda_S/40$). Equation (32) then gives $\Delta Y_c = 0.161\lambda_S$, close to that predicted in Fig. 6(a).

The selection of $y_c$ can influence the results. By examining $y_c$ from $\lambda_S/200$ to $\lambda_S/20$, Fig. 6(b) shows that $\Delta Y_c$ decreases very slowly as $y_c$ increases. Therefore, this parameter is not critical as soon as $y_c \ll \lambda_S$ is assured.

However, $P_1$ and $P_2$ selected in the above are distinctively different in their $\Phi a^2$ values. And the conclusions do not stand if $\Phi_1 a_1^2$ is close to $\Phi_2 a_2^2$. For example, by selecting the 6-$\mu$m and 5-$\mu$m PS particles, respectively, as $P_1$ and $P_2$, it is difficult to separate them using the current field, as Fig. 6(c) indicates a $\Delta Y_c$ of only $0.022\lambda_S$. Lowering the frequency $f$ can certainly increase $\Delta Y_c$, but will decrease the ARF and increase the device size, impairing the efficiency and the portability of the chip.

Before designing a separation device of this category, one needs to choose (a) the expected $\Delta Y_c$, which is highly related to the purity of the separated particles [23], and (b) the flow velocity $v_f$, which determines the throughput. The working frequency $f$ should be chosen such that $\lambda_S/4 - y_{c0} - y_c - y_a > \Delta Y_c$, and the acoustophoretic period $t_c$ can be determined through Eq. (33) or more accurately, Eq. (32). This requires to have a rough estimation of the driving pressure, typical values of which can be referred to Refs. [18] and [39], while the real pressure can be calibrated by measuring the SAW amplitude using a laser vibrometer [18]. Consequently, the IDT aperture size can be determined as $W_{IDT} = v_f \times t_c$, i.e., higher throughput requires wider IDTs.

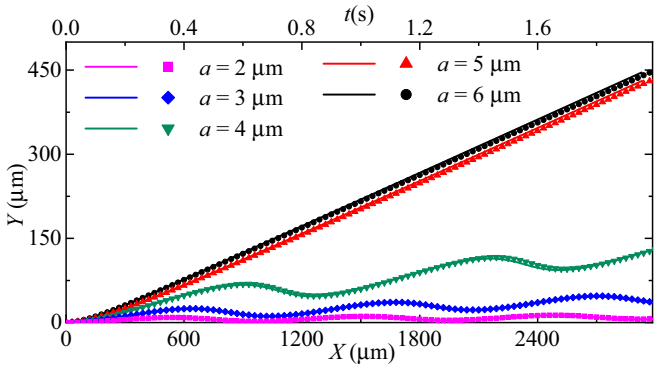


FIG. 7. The particle trajectories in a TaSSAW device (solid lines) of $\theta = 9^\circ$, $\varphi = 0$ and a PM-SSAW (dotted lines) device of $\dot{\varphi} = 9.8$ rad/s and $\varphi_0 = 0$.

### B. Comparison between TaSSAW and PM-SSAW

By reviewing Eq. (11), $|b_d/b_l|$ is independent of $v_f$ in PM-SSAW devices, thus change in $v_f$ does not shift a particle from one mode to another [40]. Equations (15) and (18) further indicate that the trajectories as functions of $t$ are independent of $v_f$. In comparison, a TaSSAW device relies on the flow drag to counterbalance the ARF, and the particle moving pattern and trajectory are sensitive to $v_f$ [23]. However, the tilted angle $\theta$ cannot be changed once a TaSSAW device is prepared, while the phase modulation rate $\dot{\varphi}$ of a PM-SSAW chip can be easily tuned. Therefore, PM-SSAW should be preferable to allow easy design tasks and delicate in-experiment optimizations. However, in PM-SAW devices, each type of particles occupies a band area as is observed in Fig. 4(c), thus a wider channel width is usually required.

The performance of a PM-SSAW or TaSSAW chip can be reproduced with a device of the other category. For example, if $\theta$ in TaSSAW and $\dot{\varphi}$ in PM-SSAW are related by $\sin\theta = \dot{\varphi}/(2k_y v_f)$, then a particle moves in similar patterns in both devices as soon as all other chip parameters are identical. In fact, the trajectories can be slightly different, since the second term on the right side of Eq. (15) is equivalent for the two fields in the $(x, y, z)$ coordinate, but different in $(X, Y, z)$. Specifically, $Y$ for PM-SSAW is the mentioned term plus $\dot{\varphi}t/2k_y$, whereas for TaSSAW it is the term rotated by $\sin^{-1}[\dot{\varphi}/(2k_y v_f)]$. By taking the parameters $f = 13.3$ MHz, $p_1 = p_2 = 100$ kPa and $v_f = 1.5$ mm/s, we let PS beads of different radii enter a TaSSAW field of $\theta = 9^\circ$, $\varphi = 0$ and a PM-SSAW field of $\dot{\varphi} = 9.8$ rad/s and $\varphi_0 = 0$ at $X = 0$, $Y = 0$. Since the condition $\sin\theta = \dot{\varphi}/(2k_y v_f)$ is met, in Fig. 7 the PM-SSAW trajectories are close to the TaSSAW ones.

From Figs. 2–7, it is convenient to separate two types of particles by moving them in different patterns, i.e., one in locked mode and the other in drift mode. Equations (20) and (24) indicate that particles of equivalent $\Phi a^2$ values fall into the same mode in a given PM-SSAW or TaSSAW field, although they can still be separated as soon as their $\Phi$ or $a$ values are different. In comparison, SSAW chips cannot separate particles of equivalent $\Phi a^2$ values.

### C. Design of TaSSAW and PM-SSAW devices

Optimization of TaSSAW and PM-SSAW chips can be tricky, since particles can move in different patterns therein. In these cases, all trajectories tend to have approximately constant slopes, and the slope difference between two particle lines is roughly proportional to the separation distance [19,23]. For a "locked" particle, Eq. (18) gives the slope in $(x, y, z)$ as $K_{\text{locked}} = \dot{\varphi}/(2v_f k_y \cos\theta)$. In a drift mode, the trajectory oscillates around a straight line, whose slope [12,19] is $K_{\text{drift}} = K_{\text{locked}} - \beta/\cos\theta$. In the $(x, y, z)$ coordinate, the slope difference is then $\Delta K = \beta_2/\cos\theta$, with $\beta_2 = (b_{d,2}^2 - b_{l,2}^2)^{\frac{1}{2}}$, where $b_{i,j}$ refers to the parameter $b_i$ of the particle $j$.

As we assume $P_1$ have bigger $\Phi a^2$ than $P_2$, it is natural to separate them by keeping $P_1$ "locked" ($b_{d,1} < b_{l,1}$) and let $P_2$ "drift" ($b_{d,2} > b_{l,2}$). Obviously, increasing $\Delta K = \beta_2/\cos\theta$ expands the separation distance $\Delta Y_c$. Considering Eq. (11), one can increase the phase modulation rate $\dot{\varphi}$ or the tilted angle $\theta$ to achieve optimized $\Delta K$. However, $\beta_1 = (b_{l,1}^2 - b_{d,1}^2)^{\frac{1}{2}}$ is to decline as $\beta_2$ goes up, and it is possible that $P_1$ is shifted to the drift mode. If that happens, then we have $\Delta K = (\beta_2 - \beta_1)/\cos\theta$ with $\beta_1$ updated as $(b_{d,1}^2 - b_{l,1}^2)^{\frac{1}{2}}$, and further increasing $\beta_2$ (and in turn $\beta_1$) decreases $\Delta K$. Therefore, an optimal $\Delta K$ occurs at the transition condition of $P_1$, i.e., $b_{d,1} = b_{l,1}$. In practice, it is safer to have $b_{d,1} \lessapprox b_{l,1}$, ensuring $P_1$ being "locked." Increasing $\beta_2$ can also be done by lowering the flow velocity, the frequency, or the pressure amplitude, which in turn impairs the throughput, the portability and the efficiency of the device.

By referring to Eqs. (21), (22), and (23), $\Delta Y_c$ in a TaSSAW field can be determined as

$$\begin{aligned}\Delta Y_c &= [(y_{\text{locked}} - y_{\text{drift}}^{(+)})\cos\theta - y_a]_{x=W_{\text{IDT}}} \\ &= \beta_2 W_{\text{IDT}} - y_a - \delta_{y,2}^{+}\cos\theta \\ &\quad + \frac{1}{k_y}\left[\tan^{-1}\frac{\beta_1 - b_{l,1}}{b_{d,1}} - \xi_{1,2}(y_0, \varphi_0)\right]\cos\theta. \end{aligned} \tag{34}$$

For a PM-SSAW device, from Eqs. (25) and (26), we have

$$\begin{aligned}\Delta Y_c &= [y_{\text{locked}}^{(-)} - y_{\text{drift}}^{(+)} - y_a]_{x=W_{\text{IDT}}} \\ &= \beta_2 W_{\text{IDT}} - y_a - \delta_{y,2}^{+} - \delta_{y,2}^{-} \\ &\quad + \frac{1}{k_y}\left(\tan^{-1}\frac{\beta_1}{b_{d,1}} - \pi\right). \end{aligned} \tag{35}$$

Again, the field pressure should be roughly estimated beforehand, and can be calibrated in experiments [18,39]. In designing these chips, one should first set the flow velocity $v_f$ according to the required throughput. Then, $\theta$ or $\dot{\varphi}$ should be adjusted to have $b_{d,1} \lessapprox b_{l,1}$. During this step, a higher frequency $f$ is usually preferred, since it helps to increase the ARF, and reduce the width of particle bands in the $y$ direction. Finally, $W_{\text{IDT}}$ can be determined using Eqs. (34) and (35).

One may concern if the terms added to $\beta_2 W_{\text{IDT}}$ in Eqs. (34) and (35) make it invalid that the maximum slope difference produces optimal $\Delta Y_c$. Here, we compare $\Delta K$ and $\Delta Y_c$ in the separation of PS beads. With the field parameters $f = 13.3$ MHz, $v_f = 1.5$ mm/s, $W_{\text{IDT}} = 9$ mm, $a_1 = 5$ $\mu$m, $a_2 = 3$ $\mu$m and $p_1 = p_2 = 80$, 100, and 120 kPa, we examine $\Delta K$ and $\Delta Y_c$ as functions of $\theta$ for a TaSSAW device and of $\dot{\varphi}$ for a PM-SSAW chip, with the results (in arbitrary units) given in Figs. 8(a) and 8(b), respectively. Although the locations of each pair of $\Delta K$ and $\Delta Y_c$ peaks are slightly different, one can still conclude that $\Delta K$ is a good predictor of $\Delta Y_c$. Here, the

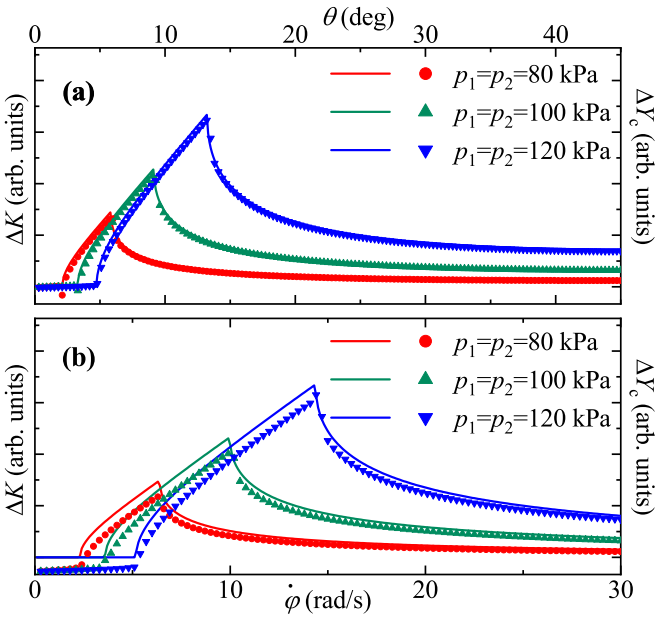


FIG. 8. Comparison between the trajectory slope differences $\Delta K$ (solid lines) and the final separation distances $\Delta Y_c$ (dotted lines) as functions of (a) $\theta$ in TaSSAW fields and (b) $\dot{\varphi}$ in PM-SSAW fields for 3- and 5-$\mu$m PS particles. $f = 13.3$ MHz, $v_f = 1.5$ mm/s, $W_{IDT} = 9$ mm.

$\theta$ and $\dot{\varphi}$ locations where $\Delta K$ maximizes are exactly when $P_1$ transit between "locked" and "drift."

Dexterous particle separations can be developed by employing the theories here. For example, the two-step particle filtration protocol by Pelton *et al.* [37] can be easily achieved by adjusting the critical radius $a_c$ in Eq. (20) for TaSSAW and that in Eq. (24) for PM-SSAW.

### D. Design of pSSAW devices

From Fig. 5, pSSAW requires SWR to be close to 1 to achieve separation, as the ARF of a traveling wave is much smaller than that of a standing wave of equivalent magnitude [35]. That is, the radio $p_1/p_2$ should be high enough to make the drifting part comparable to the locking part in their contributions to the overall ARF, as is referred to in Eq. (6). Perhaps due to this reason, pSSAW is not widely used for particle separations.

However, a pSSAW device can have its unique advantages if delicately designed and operated. As we consult to Fig. 5(b), it can be easy to separate multiple types of particles with one pSSAW device. For example, while moving in locked modes, particles can have different final $y$ locations according to Eq. (29). By respectively selecting $C(y_0, \varphi_0) < 0$ and $C(y_0, \varphi_0) > 0$ for two types of "locked" particles, $\Delta Y_c$ in pSSAW is approximately $\lambda_S/2$, which doubles that of a SSAW device. Therefore, multiple objective separations can be achieved by putting two types of particles in different locked modes, while others in drift modes. One remembers that, the final locations of all "locked" particles in TaSSAW or PM-SSAW fields are close to each other, see Figs. 3(b) and 4(b).

In designing such devices, one first determines $v_f$ according to the required throughput. Then, the transition condition $|b_d/b_l| = |\mathrm{Im}(f_2)/\Phi| l/(l^2-1)$ helps to determine the frequency $f$ and the SWR $l$, such that the locked and drift modes can be assigned to different particles. A lower $f$ is recommended if two types of particles are expected to move in different locked modes, e.g., $y^{(0)}_{\mathrm{locked}}$ and $y^{(1)}_{\mathrm{locked}}$, since the entire $y$ space allowed for them is limited by $\lambda_S/2$. But according to Eq. (18), a lower $f$ will require a longer period for a "locked" particle to reach its final $y$ position. For separating particles in drift modes, the slope difference analysis is similar to that in Sec. IV C. For example, if $P_1$ and $P_2$ are both in drift modes, then the slope difference should be $\Delta K = \beta_1 - \beta_2$. Otherwise, if $P_1$ is in "drift" and $P_2$ is "locked," then $\beta_1$ should be maximized as soon as $b_{l,2} \gtrapprox |b_{d,2}|$. It is difficult to give an analytical $W_{IDT}$ here, and one needs to calculate the particle trajectories using Eqs. (18) and (31) to check the design.

### E. Validation of the theory

In the theory, the flow velocity $v_f$ is assumed uniform along the channel width, but is usually a parabolic function in real cases [43]. However, figuring out the analytic expressions of particle trajectories by considering uneven fluid flow can be very tedious. Here, we use FE simulations to discuss the applicability of the theories.

For separation purposes, we are only interested in the $X$-$Y$ plane, specifically, in the fluid domain illustrated in Fig. 1(b). Following the previous discussions, varied flow velocity does not change the moving patterns of particles in SSAW, PM-SSAW, and pSSAW fields, therefore, we here only study the TaSSAW case to demonstrate.

For example, we consider separating 6-$\mu$m ($P_1$) and 3-$\mu$m ($P_2$) PS particles using a TaSSAW chip of $f = 13.3$ MHz and $p_1 = p_2 = 100$ kPa, and expect the separation distance $\Delta Y_c = 400$ $\mu$m and the throughput corresponding to an average flow rate $\overline{v}_f = 1.5$ mm/s. The width of the channel is then designed as $W = 800$ $\mu$m, i.e., across $Y = -400$ to 400 $\mu$m. The actual flow velocity is described as [43] $v_f(Y) = 3\overline{v}_f(W^2 - 4Y^2)/2W^2$, i.e., $v_f$ has small values but high $Y$-direction gradients near the boundaries. Considering this, we use only 60% of the channel width, i.e., the working area is designed between $Y = -240$ to 240 $\mu$m. The average flow velocity within this area, $\overline{v}'_f = 1.32\overline{v}_f = 1.98$ mm/s, is used as the equivalently uniform $v_f$ for theoretical trajectory predictions.

To place $P_1$ in locked mode and achieve an optimal separation distance, it is essential that $b_{d,1} \lessapprox b_{l,1}$, giving a critical tilted angle $\theta_c = 9.98°$ according to Eq. (20), and we select $\theta = 0.9\theta_c = 9°$. Finally, Eq. (34) gives $W_{IDT} \geqslant 2900$ $\mu$m, and we choose $W_{IDT} = 3000$ $\mu$m. With this design, the critical radius is estimated as $a_c = 5.7$ $\mu$m.

The top view of the chip is then given in Fig. 9(a). Where three inlets and three outlets are designed. Inlets 1 and 3 are used to generate sheath flows to prefocus the particles to a trap. The generated TaSSAW fields is given in Fig. 9(b), where the field fluctuation due to limited IDT apertures [44] can be clearly identified along the wave fronts. The flow field is depicted in Fig. 9(c), where the black streamlines show the

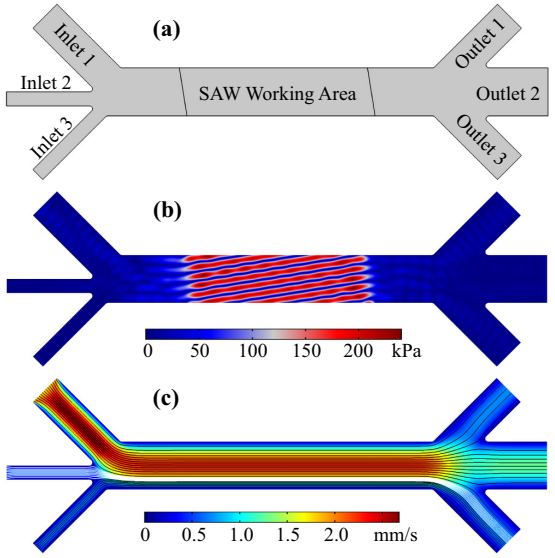


FIG. 9. (a) Top view of the simulated fluid domain; (b) the generated TaSSAW field of $f=13.3$ MHz, $\theta=9°$, $p_1=p_2=100$ kPa, and $W_{IDT}=3000$ $\mu$m; and (c) the flow field with a $Y$-averaged flow velocity $\overline{v}_f=1.5$ mm/s.

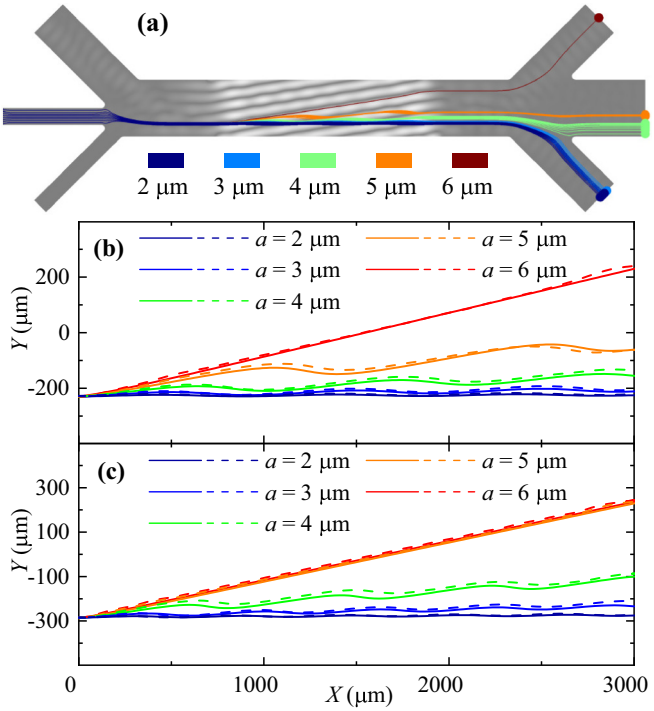


FIG. 10. (a) FE simulated tracking of $a=2$, 3, 4, 5, 6 $\mu$m PS particles, the grayscale is the distribution of the TaSSAW field of $f=13.3$ MHz, $\theta=9°$, $p_1=p_2=100$ kPa, $W_{IDT}=3000$ $\mu$m, and $\overline{v}_f=1.5$ mm/s; (b) comparisons between the simulated (dashed lines) and predicted (solid lines) trajectories; (c) $f$, $p_1$, and $\overline{v}_f$ are changed to 19.97 MHz, 120 kPa, and 2 mm/s.

sheath flows and the white lines come from inlet 2, the particle inlet.

With the fields in Figs. 9(b) and 9(c), we then perform particle tracking analysis by accounting for both ARF and DF acting on the beads. To better illustrate the results, apart from the $P_1$ and $P_2$ particles we also introduce 2-, 4-, and 5-$\mu$m PS beads from inlet 2. In the tracking results in Fig. 10(a), the biggest particles $P_1$ obviously follow locked mode motions, and move to the upper outlet (outlet 1), the $P_2$ particles cross several potential barriers and reach the lower outlet (outlet 3). The smallest particles ($a=2$ $\mu$m) also go to outlet 3, as is expected. The medium size ones ($a=4$ and 5 $\mu$m) are also below the critical radius, and they move in drift modes to the middle outlet (outlet 2). It should be mentioned that, each type of particle actually occupies a band area in the $Y$ direction, and smaller particles have wider bands. This is because the prefocusing process is not ideal, it cannot aggregate all particles exactly at the same $Y$ position. In other words, this demonstrates the influence of the initial position $y_0$, which is similar to the phenomenon observed in BAW acoustofluidics [42].

For each particle size, we compare the simulated trajectory of a single particle with that predicted using Eqs. (15) and (18) in Fig. 10(b). It is observed that, the final separation distance between $P_1$ and $P_2$ is about 420 $\mu$m, slightly beyond our expectation. For particles in drift mode, e.g., the 4-$\mu$m and 5-$\mu$m ones, their lateral displacements determined from simulations are slightly bigger than theoretical predictions. This is because their initial positions are away from the center of the channel, and the actual flow velocity they experience is lower than $\overline{v}_f'$, i.e., the influence of the fluid flow is slightly overestimated in the theory. For the 6-$\mu$m particles, they move in the locked mode, and the simulated trajectory matches well with the theory. At the end of the 3000 $\mu$m journey, the simulated path of the 6-$\mu$m particles slightly deviates from the theory, which is possibly due to the non-ideal cutoff of the field at the IDT edges [44].

In the second demonstration, 5-$\mu$m ($P_1$) and 3-$\mu$m ($P_2$) PS particles are expected to be separated by 400 $\mu$m. Here, we choose $f=19.97$ MHz, $p_1=p_2=120$ kPa, $\overline{v}_f=2$ mm/s, and $W=1000$ $\mu$m. In this case, $\overline{v}_f'$ between $Y=-300$ to 300 $\mu$m is about 2.64 mm/s, giving a critical $\theta_c=11.24°$. Then, $\theta=0.9\theta_c=10°$ induces $W_{IDT}\geqslant 2700$ $\mu$m. By selecting $W_{IDT}=3000$ $\mu$m, the simulated trajectories of $a=2, 3, 4, 5, 6$ $\mu$m beads and theoretical predictions are compared in Fig. 10(c), where good matchings are observed for particles of each size. $P_1$ and $P_2$ are finally separated by about 460 $\mu$m, well above the required.

In the above simulations, the wall corrections are negligible. For example, in Fig. 10(b) the designed particle trajectories are at least 160 $\mu$m from the walls. For the biggest particle used in the calculations ($a=6$ $\mu$m), the parallel and perpendicular correction factors are 1.022 and 1.044, respectively. One should be notified that, in real cases the channel should also be high enough to allow corresponding correction factor be small enough.

Some previous published experimental findings can be reproduced using the current theory. For example, the curve patterns in Fig. 8(a) are similar to the results reported by Ding *et al.* [11]. In their Fig. 2, PS beads of 9.9-$\mu$m diameter had a lateral migration of ~130 $\mu$m more than 7.3-$\mu$m beads. By using exactly the same parameters, $\Delta Y_c$ obtained from Eq. (34) is 157 $\mu$m, agreeing well with their value if

experimental uncertainties are considered. In their Fig. 3B, at $X = 1600$ $\mu$m the lateral migration of 10- and 15-$\mu$m beads are approximately 380 and 220 $\mu$m, respectively. By using Eqs. (15) and (18), theoretically estimated results are about 400 and 200 $\mu$m, respectively. In the study by Simon *et al.* [13], a PM-SSAW device is used for particle separation experiments. In their Fig. 5(b), at $t = 0.64$ s PS particles of 10- and 15-$\mu$m migrated about 105 and 30 $\mu$m, respectively. By adopting the same group of parameters, these distances are estimated as 100 and 29 $\mu$m by Eqs. (25) and (26).

## V. CONCLUSION

We have established a theoretical framework to describe the acoustophoretic motions of Rayleigh particles in different types of counterpropagating SAW fields. Based on this framework, we provide theory-based design protocols for different particle separation chips.

Generally, the theory can be used to predict particle trajectories in SSAW, TaSSAW, PM-SSAW, and pSSAW fields, while in the latter three the particle motions can be in "locked" or "drift" modes. The moving pattern of a particle can be influenced by the flow velocity in a TaSSAW device, but it is not that crucial in PM-SSAW and pSSAW chips. In devices except PM-SSAW ones, each kind of particles can formulate a well predicted line in the channel. In PM-SSAW devices, the randomly distributed initial phase experienced by particle individuals make the particle lines expand to band areas.

These findings enable us to optimize designs of corresponding particle separation chips. Specifically, we offer strategies for determining the frequency, the flow velocity, the phase modulation rate, the tilted angle, and the aperture sizes of IDTs. FE simulations demonstrate that, the proposed protocols work well when consider the parabolic-distributed flow velocity as an equivalent uniform one. By employing the methods given here, it is not only convenient to design new chips or optimize existing ones, but also possible to explore more delicate functionalities using counterpropagating SAWs, such as multiple objective particle separations.

## ACKNOWLEDGMENTS

This work was supported by the National Natural Science Foundation of China (Grants No. 81627802, No. 11934009, No. 11974179, No. 11874216, No. 11774166, No. 11774168, and No. 11674173), and the Fundamental Research Funds for the Central Universities. Dr. X.G. is a Fellow at the Collaborative Innovation Center for Cardiovascular Disease Translational Medicine, Nanjing Medical University.

## APPENDIX A: FE SIMULATION METHODS

The modeling methods and convergence test procedures are similar to those in Ref. [21]. Here we use the model in Fig. 9 as an example to explain. The in-channel fluid is water, the particles to be manipulated are PS beads, and their material properties are listed in Table I. For simplicity, simulations are conducted within the $X$-$Y$ plane where the particles are present. Besides, thermoviscous effects of the fluid are neglected, and AS is neglected in the considered problems.

In the first step, the flow field is created in the channel. In the FE software COMSOL Multiphysics we used, this is conducted in a "stationary" study using the "creeping flow" interface. For inlets 1–3 shown in the geometry, "Inlet" boundaries are added, where the "normal inflow velocity" are 1.8, 0.3, and 0.54 mm/s, respectively. On the right side, "outlet" boundaries are used for the outlets 1–3, and zero pressure is assigned for all the outlets. For the other boundaries shown in the model, non-slip conditions are considered.

Then, we use the "pressure acoustics, frequency domain" interface to build the acoustic field in the $X$-$Y$ plane. To mimic the leaking of SAWs from the substrate, an out-of-plane wave number $k_z = k\cos\theta_R$ is applied to the SAW working area. At the two side boundaries, plane wave radiations are imposed at the working area, i.e., both the actuation regions have widths $W_{IDT}/\cos\theta$, where the "incident pressure field" conditions are employed. The channel walls are considered as "impedance" boundaries, where the acoustic impedance of PDMS, $\rho_{pm}c_{pm}$, is assigned.

Finally, particle behaviors are studied using the "particle tracing for fluid flow" interface. As the particles experience both ARF and DF, the former is evaluated through Eq. (2) using the obtained acoustic field, and the latter is calculated as $\boldsymbol{F}_{drag} = 6\pi\eta a(\boldsymbol{v}_f - \boldsymbol{v}_p)$ with the obtained flow field. Monodispersed particles of designated radii are injected into the channel from Inlet 2.

In discretizing the fluid domain, free triangular elements are used, and the element size has an upper limit $h_b = \delta/p_m$ at the boundary of the fluid domain and $50h_b$ in the bulk area. The mesh parameter $p_m$ is determined by examining a convergence parameter $C(g)$ [21]. In all the models considered here, $p_m$ is chosen as 1, ensuring $C(g)$, which is calculated using a reference field having $p_m = 3$, being lower than 0.005 for the in-channel acoustic fields and velocity fields.

## APPENDIX B: PARAMETER $\delta_y^{\pm}$ IN EQS. (22) AND (26)

For the drift-mode particle trajectory in Eq. (15), we further consider a straight trajectory line,

$$y_{d0} = \frac{\dot{\varphi}t}{2k_y} - \beta v_f t, \tag{B1}$$

which is equivalent to the expression reported by Riaud *et al.* [19]. The distance between the two lines, $\Delta y = y - y_{d0}$, is evaluated, as

$$\Delta y = \frac{\varphi_0}{2k_y} + \beta v_f t + \frac{1}{k_y}\tan^{-1}\left\{\frac{\beta}{b_d}\tan\left[\xi_1(y_0,\varphi_0) - \beta k_y v_f t\right] - \frac{b_l}{b_d}\right\}. \tag{B2}$$

For simplicity, we let $\zeta = \tan\left[\beta k_y v_f t - \xi_1(y_0,\varphi_0)\right]$, which leads Eq. (B2) to the form

$$k_y\Delta y - \frac{\varphi_0}{2} = \beta k_y v_f t - \tan^{-1}\left(\frac{\beta}{b_d}\zeta + \frac{b_l}{b_d}\right). \tag{B3}$$

We then assume $\delta_y = \Delta y - \varphi_0/2k_y - \xi_1(y_0, \varphi_0)/k_y$, which turns Eq. (B3) into

$$k_y\delta_y = \tan^{-1}\zeta - \tan^{-1}\left(\frac{\beta}{b_d}\zeta + \frac{b_l}{b_d}\right). \tag{B4}$$

Since $\beta = |b_d^2 - b_l^2|^{\frac{1}{2}}$ and $|b_d/b_l| > 1$, we further assume $\beta = b_d\cos\alpha$ and $b_l = b_d\sin\alpha$. Equation (B4) is then rewritten as

$$k_y\delta_y = \tan^{-1}\frac{\zeta(1-\cos\alpha) - \sin\alpha}{\zeta^2\cos\alpha + \zeta\sin\alpha + 1} = \tan^{-1}\Omega. \tag{B5}$$

In obtaining Eq. (B5), trigonometric relationship $\tan^{-1}A - \tan^{-1}B = \tan^{-1}[(A-B)/(1+AB)]$ is used. Since $\tan^{-1}(\cdot)$ is a monotonic increasing function, the maxima and minima of $\delta_y$ (and in turn $\Delta y$) are determined by those of $\Omega$. By letting $d\Omega/d\zeta = 0$, these maxima and minima points could be found at

$$\zeta = \frac{\sin\alpha\cos\alpha \pm [2\cos\alpha(1-\cos\alpha)]^{1/2}}{\cos\alpha(1-\cos\alpha)}. \tag{B6}$$

By putting Eq. (B6) into Eq. (B5), the boundary correction term in Eq. (22) is obtained as

$$\delta_y^{\pm} = \frac{1}{k_y}\tan^{-1}\frac{(1-\cos\alpha)^{3/2}}{(8\cos\alpha)^{1/2} \pm (1+\cos\alpha)^{3/2}}. \tag{B7}$$

For drift-mode trajectories in PM-SSAW, $\Delta y = y - y_{d0}$ can also be contributed by the initial phase $\varphi_0$ assigned to different particle individuals. Considering the definition of $\xi_1(y_0, \varphi_0)$ by Eq. (14), we rewrite Eq. (B4) as

$$k_y\Delta y - k_y\delta_y = \frac{\varphi_0}{2} + \tan^{-1}\left[\frac{b_d}{\beta}\tan\left(k_y y_0 - \frac{\varphi_0}{2}\right) + \frac{b_l}{\beta}\right]. \tag{B8}$$

Let $\zeta' = \tan(\varphi_0/2 - k_y y_0)$ and $\delta_y' = \Delta y - \delta_y - y_0$, one then obtains

$$k_y\delta_y' = \tan^{-1}\zeta' - \tan^{-1}\left(\frac{b_d}{\beta}\zeta' - \frac{b_l}{\beta}\right), \tag{B9}$$

and in turn,

$$k_y\delta_y' = \tan^{-1}\zeta' - \tan^{-1}\frac{\zeta' - \sin\alpha}{\cos\alpha}. \tag{B10}$$

Benefiting from the trigonometric relationship mentioned in the above, we have

$$k_y\delta_y' = \tan^{-1}\frac{\sin\alpha - \zeta'(1-\cos\alpha)}{\zeta'^2 - \zeta'\sin\alpha + \cos\alpha} = \tan^{-1}\Omega'. \tag{B11}$$

By checking $d\Omega'/d\zeta' = 0$, the maxima and minima of $\delta_y'$ (and in turn $\Delta y - \delta_y$) are found at

$$\zeta' = \frac{\sin\alpha \mp [2\cos\alpha(1-\cos\alpha)]}{1-\cos\alpha}. \tag{B12}$$

By putting Eq. (B12) into Eq. (B11), the contribution of varied $\varphi_0$ in the boundary line expression is

$$\delta_y'^{\pm} = \frac{1}{k_y}\tan^{-1}\frac{(1-\cos\alpha)^{3/2}}{(8\cos\alpha)^{1/2} \mp (1+\cos\alpha)^{3/2}} = \delta_y^{\mp}, \tag{B13}$$

which appears on the right side of Eq. (26).


[1] M. Wu, A. Ozcelik, J. Rufo, Z. Wang, R. Fang, and T. J. Huang, Acoustofluidic separation of cells and particles, Microsyst. Nanoeng. **5**, 32 (2019).

[2] J. Shi, H. Huang, Z. Stratton, Y. Huang, and T. J. Huang, Continuous particle separation in a microfluidic channel via standing surface acoustic waves (SSAW), Lab Chip **9**, 3354 (2009).

[3] J. Friend and L. Y. Yeo, Microscale acoustofluidics: Microfluidics driven via acoustics and ultrasonics, Rev. Mod. Phys. **83**, 647 (2011).

[4] X. Ding, P. Li, S.-C. S. Lin, Z. S. Stratton, N. Nama, F. Guo, D. Slotcavage, X. Mao, J. Shi, F. Costanzo, and T. J. Huang, Surface acoustic wave microfluidics, Lab Chip **13**, 3626 (2013).

[5] G. Destgeer, K. H. Lee, J. H. Jung, A. Alazzam, and H. J. Sung, Continuous separation of particles in a PDMS microfluidic channel via traveling surface acoustic waves (TSAW), Lab Chip **13**, 4210 (2013).

[6] Y. Ai, C. K. Sanders, and B. L. Marrone, Separation of *Escherichia coli* bacteria from peripheral blood mononuclear cells using standing surface acoustic waves, Anal. Chem. **85**, 9126 (2013).

[7] G. Simon, Y. Pailhas, M. A. B. Andrade, J. Reboud, J. Marques-Hueso, M. P. Y. Desmulliez, J. M. Cooper, M. O. Riehle, and A. L. Bernassau, Particle separation in surface acoustic wave microfluidic devices using reprogrammable, pseudo-standing waves, Appl. Phys. Lett. **113**, 044101 (2018).

[8] J. W. Ng, D. J. Collins, C. Devendran, Y. Ai, and A. Neild, Flow-rate-insensitive deterministic particle sorting using a combination of traveling and standing surface acoustic waves, Microfluid. Nanofluid. **20**, 151 (2016).

[9] T. Hasegawa and K. Yosioka, Acoustic-radiation force on a solid elastic sphere, J. Acoust. Soc. Am. **46**, 1139 (1969).

[10] H. Bruus, Acoustofluidics 7: The acoustic radiation force on small particles, Lab Chip **12**, 1014 (2012).

[11] X. Ding, Z. Peng, S.-c. S. Lin, M. Geri, S. Li, P. Li, Y. Chen, M. Dao, S. Suresh, and T. J. Huang, Cell separation using tilted-angle standing surface acoustic waves, Proc. Natl. Acad. Sci. USA **111**, 12992 (2014).

[12] J. Lee, C. Rhyou, B. Kang, and H. Lee, Continuously phase-modulated standing surface acoustic waves for separation of particles and cells in microfluidic channels containing multiple pressure nodes, J. Phys. D-Appl. Phys. **50**, 165401 (2017).

[13] G. Simon, M. A. B. Andrade, J. Reboud, J. Marques-Hueso, M. P. Y. Desmulliez, J. M. Cooper, M. O. Riehle, and A. L. Bernassau, Particle separation by phase modulated surface acoustic waves, Biomicrofluidics **11**, 054115 (2017).

[14] D. J. Collins, T. Alan, and A. Neild, Particle separation using virtual deterministic lateral displacement (VDLD), Lab Chip **14**, 1595 (2014).

[15] G. Liu, F. He, X. Li, H. Zhao, Y. Zhang, Z. Li, and Z. Yang, Multi-level separation of particles using acoustic

radiation force and hydraulic force in a microfluidic chip, Microfluid. Nanofluid. **23**, 23 (2019).
[16] C. Devendran, N. R. Gunasekara, D. J. Collins, and A. Neild, Batch process particle separation using surface acoustic waves (SAW): Integration of traveling and standing SAW, RSC Adv. **6**, 5856 (2016).
[17] T. Hasegawa, Acoustic radiation force on a sphere in a quasi-stationary wave field–theory, J. Acoust. Soc. Am. **65**, 32 (1979).
[18] S. Liu, Z. Ni, G. Xu, X. Guo, J. Tu, H. Bruus, and D. Zhang, Two-Dimensional Mapping Separating the Acoustic Radiation Force and Streaming in Microfluidics, Phys. Rev. Appl. **11**, 044031 (2019).
[19] A. Riaud, W. Wang, A. L. P. Thai, and V. Taly, Mechanical Characterization of Cells and Microspheres Sorted by Acoustophoresis with in-Line Resistive Pulse Sensing, Phys. Rev. Appl. **13**, 034058 (2020).
[20] N. Nama, R. Barnkob, Z. Mao, C. J. Kähler, F. Costanzo, and T. J. Huang, Numerical study of acoustophoretic motion of particles in a PDMS microchannel driven by surface acoustic waves, Lab Chip **15**, 2700 (2015).
[21] Z. Ni, C. Yin, G. Xu, L. Xie, J. Huang, S. Liu, J. Tu, X. Guo, and D. Zhang, Modelling of SAW-PDMS acoustofluidics: Physical fields and particle motions influenced by different descriptions of the PDMS domain, Lab Chip **19**, 2728 (2019).
[22] M. Ahmad, A. Bozkurt, and O. Farhanieh, Evaluation of acoustic-based particle separation methods, World J. Eng. **16**, 823 (2019).
[23] G. Liu, F. He, Y. Li, H. Zhao, X. Li, H. Tang, Z. Li, Z. Yang, and Y. Zhang, Effects of two surface acoustic wave sorting chips on particles multi-level sorting, Biomed. Microdevices **21**, 59 (2019).
[24] R. Barnkob, N. Nama, L. Ren, T. J. Huang, F. Costanzo, and C. J. Kähler, Acoustically Driven Fluid and Particle Motion in Confined and Leaky Systems, Phys. Rev. Appl. **9**, 014027 (2018).
[25] D. J. Collins, R. O'Rorke, C. Devendran, Z. Ma, J. Han, A. Neild, and Y. Ai, Self-Aligned Acoustofluidic Particle Focusing and Patterning in Microfluidic Channels from Channel-Based Acoustic Waveguides, Phys. Rev. Lett. **120**, 074502 (2018).
[26] R. Barnkob, P. Augustsson, T. Laurell, and H. Bruus, Acoustic radiation- and streaming-induced microparticle velocities determined by microparticle image velocimetry in an ultrasound symmetry plane, Phys. Rev. E **86**, 056307 (2012).
[27] J. Happel and H. Brenner, *Low Reynolds Number Hydrodynamics with Special Applications to Particulate Media* (Martinus Nijhoff Publishers, The Hague, 1983).
[28] P. B. Muller, R. Barnkob, M. J. H. Jensen, and H. Bruus, A numerical study of microparticle acoustophoresis driven by acoustic radiation forces and streaming-induced drag forces, Lab Chip **12**, 4617 (2012).
[29] P. B. Muller, M. Rossi, A. G. Marín, R. Barnkob, P. Augustsson, T. Laurell, C. J. Kähler, and H. Bruus, Ultrasound-induced acoustophoretic motion of microparticles in three dimensions, Phys. Rev. E **88**, 023006 (2013).
[30] J. T. Karlsen and H. Bruus, Forces acting on a small particle in an acoustical field in a thermoviscous fluid, Phys. Rev. E **92**, 043010 (2015).
[31] J. Leão Neto and G. Silva, Acoustic radiation force and torque exerted on a small viscoelastic particle in an ideal fluid, Ultrasonics **71**, 1 (2016).
[32] L. V. King, On the acoustic radiation pressure on spheres, Proc. R. Soc. Lond. A **147**, 212 (1934).
[33] K. Yosioka and Y. Kawasima, Acoustic radiation pressure on a compressible sphere, Acustica **5**, 167 (1955).
[34] L. P. Gor'kov, On the forces acting on a small particle in an acoustical field in an ideal fluid, Sov. Phys.–Dokl. **6**, 773 (1962).
[35] M. Settnes and H. Bruus, Forces acting on a small particle in an acoustical field in a viscous fluid, Phys. Rev. E **85**, 016327 (2012).
[36] S. Liang, W. Chaohui, and H. Qiao, Force on a compressible sphere and the resonance of a bubble in standing surface acoustic waves, Phys. Rev. E **98**, 043108 (2018).
[37] M. Pelton, K. Ladavac, and D. G. Grier, Transport and fractionation in periodic potential-energy landscapes, Phys. Rev. E **70**, 031108 (2004).
[38] G. Xu, Z. Ni, X. Chen, J. Tu, X. Guo, H. Bruus, and D. Zhang, Acoustic Characterization of Polydimethylsiloxane for Microscale Acoustofluidics, Phys. Rev. Appl. **13**, 054069 (2020).
[39] S. Liu, G. Xu, Z. Ni, X. Guo, L. Luo, J. Tu, and D. Zhang, Quantitative assessment of acoustic pressure in one-dimensional acoustofluidic devices driven by standing surface acoustic waves, Appl. Phys. Lett. **111**, 043508 (2017).
[40] C. Rhyou, S. Park, and H. Lee, Optimal rate for continuous phase modulation in standing surface acoustic waves, J. Mech. Sci. Technol. **33**, 3819 (2019).
[41] F. Jacobsen and P. M. l. Juhl, *Fundamentals of General Linear Acoustics* (John Wiley & Sons, New York, NY, 2013).
[42] T. Yang, V. Vitali, and P. Minzioni, Acoustofluidic separation: Impact of microfluidic system design and of sample properties, Microfluid. Nanofluid. **22**, 44 (2018).
[43] H. Bruus, Acoustofluidics 1: Governing equations in microfluidics, Lab Chip **11**, 3742 (2011).
[44] A. Fakhfouri, C. Devendran, T. Albrecht, D. J. Collins, A. Winkler, H. Schmidt, and A. Neild, Surface acoustic wave diffraction driven mechanisms in microfluidic systems, Lab Chip **18**, 2214 (2018).